



Measurement of forward W and Z boson production in association with jets in proton-proton collisions at $\sqrt{s} = 8 \text{ TeV}$

The LHCb collaboration[†]

Abstract

The production of W and Z bosons in association with jets is studied in the forward region of proton-proton collisions collected at a centre-of-mass energy of 8 TeV by the LHCb experiment, corresponding to an integrated luminosity of $1.98 \pm 0.02 \text{ fb}^{-1}$. The W boson is identified using its decay to a muon and a neutrino, while the Z boson is identified through its decay to a muon pair. Total cross-sections are measured and combined into charge ratios, asymmetries, and ratios of W +jet and Z +jet production cross-sections. Differential measurements are also performed as a function of both boson and jet kinematic variables. All results are in agreement with Standard Model predictions.

Published in JHEP 05 (2016) 131

© CERN on behalf of the LHCb collaboration, licence CC-BY-4.0.

[†]Authors are listed at the end of this paper.

1 Introduction

Measurements of vector boson production in association with jets in the forward region at the Large Hadron Collider (LHC) can be used to test the Standard Model (SM) and provide constraints on the parton density functions (PDFs). LHCb is the only detector at the LHC with precision tracking coverage in the forward region, allowing sensitivity to PDFs at a different range of Bjorken- x compared to ATLAS and CMS [1]. LHCb measurements typically probe PDFs at x as low as 10^{-4} and at high x [2].

This article reports total and differential cross-section measurements of W and Z production in association with jets, hereafter referred to as Wj and Zj , respectively.¹ The measurements are performed using data collected during 2012 at a centre-of-mass energy of $\sqrt{s} = 8$ TeV, corresponding to an integrated luminosity of $1.98 \pm 0.02 \text{ fb}^{-1}$. The W and Z bosons are identified through the $W \rightarrow \mu\nu_\mu$ and $Z \rightarrow \mu\mu$ decay channels. This work extends measurements of the Zj production cross-section at 7 TeV [3, 4] and ratios of the production cross-sections at 7 and 8 TeV [5]. It also complements previous studies of inclusive electroweak boson production at LHCb, where the electroweak bosons decay to muons [6–8].

This analysis makes use of the same fiducial acceptances for electroweak bosons as previously employed in Ref. [7]. For W boson decays, this corresponds to requiring that the muon has a pseudorapidity, η^μ , in the range $2.0 < \eta^\mu < 4.5$ and transverse momentum, p_T^μ , greater than 20 GeV.² For Z boson decays, both muons are required to fulfil these kinematic requirements, and in addition, the dimuon invariant mass, $M_{\mu\mu}$, is required to be in the range $60 < M_{\mu\mu} < 120$ GeV. The fiducial criteria for these measurements require at least one jet to have transverse momentum $p_T^{\text{jet}} > 20$ GeV, and jet pseudorapidity, η^{jet} , in the range $2.2 < \eta^{\text{jet}} < 4.2$. The jet is also required to be separated by a radius ΔR of 0.5 from the charged lepton(s) produced in the boson decay, where ΔR is the sum in quadrature of the difference in pseudorapidity and the difference in azimuthal angle between the jet and the lepton. In addition, the Wj measurement requires that the transverse component of the vector sum of the muon and jet momenta, $p_T^{\mu+j}$, is greater than 20 GeV. Jets are reconstructed using the anti- k_T algorithm [9], with the R parameter set to 0.5. Jet energies are defined at the hadron level, and do not include the contribution of neutrinos in the jet.

All measurements are performed for the jet with the largest transverse momentum in the event. The Wj measurement is made differentially as a function of p_T^{jet} , η^{jet} , and the pseudorapidity of the muon produced by the W boson decay, η^μ . For the Zj measurement, the differential cross-sections are determined as a function of p_T^{jet} , η^{jet} , the boson rapidity, y^Z , and the difference in azimuthal angle between the Z boson and the jet, $|\Delta\phi|$. The jet transverse momentum distributions and the $|\Delta\phi|$ distribution tend to be sensitive to higher-order effects within perturbative quantum chromodynamics (QCD) [10],

¹Here, the notation Z additionally includes contributions from virtual photon production and its interference with Z boson production, Z/γ^* .

²This article uses natural units, where the speed of light (c) and the reduced Planck constant (\hbar) are set to unity, $c = \hbar = 1$.

while measurements of the (pseudo)rapidity distributions are sensitive to the PDFs that parameterise the structure of the proton. The ratio of the W^+j to the W^-j cross-sections is measured, as is the ratio of the Wj cross-sections to the Zj cross-section. Finally, the charge asymmetry of Wj production is measured as a function of η^μ .

2 Detector and simulation

The LHCb detector [11,12] is a single-arm forward spectrometer covering the pseudorapidity range $2 < \eta < 5$, designed for the study of particles containing b or c quarks. The detector includes a high-precision tracking system consisting of a silicon-strip vertex detector surrounding the pp interaction region, a large-area silicon-strip detector located upstream of a dipole magnet with a bending power of about 4 Tm, and three stations of silicon-strip detectors and straw drift tubes placed downstream of the magnet. The tracking system provides a measurement of momentum, p , of charged particles with a relative uncertainty that varies from 0.5% at low momentum to 1.0% at 200 GeV. The minimum distance of a track to a primary vertex (PV), the impact parameter, is measured with a resolution of $(15 + 29/p_T) \mu\text{m}$, where p_T is the component of the momentum transverse to the beam, in GeV. Different types of charged hadrons are distinguished using information from two ring-imaging Cherenkov detectors. Photons, electrons and hadrons are identified by a calorimeter system consisting of scintillating-pad (SPD) and preshower detectors, an electromagnetic calorimeter and a hadronic calorimeter. Muons are identified by a system composed of alternating layers of iron and multiwire proportional chambers. The online event selection is performed by a trigger, which consists of a hardware stage, based on information from the calorimeter and muon systems, followed by a software stage, which applies a full event reconstruction.

In this paper, candidate events are required to pass the hardware trigger, which selects muons with a transverse momentum $p_T > 1.76$ GeV and the subsequent software trigger, where a muon with $p_T > 10$ GeV is required to be present. A global event cut (GEC) is also applied at the hardware stage, which requires that the number of hits in the SPD sub-detector should be less than 600.

Simulated pp collisions are generated using PYTHIA 8 [13] with a specific LHCb configuration [14]. Decays of hadronic particles are described by EVTGEN [15], in which final-state radiation is generated using PHOTOS [16]. The interaction of the generated particles with the detector, and its response, are implemented using the GEANT4 toolkit [17] as described in Ref. [18].

Results are compared to theoretical calculations performed at $\mathcal{O}(\alpha_s^2)$ in perturbative QCD using the POWHEG [10,19] and aMC@NLO [20] generators, interfaced with PYTHIA in order to simulate the parton shower, where the NNPDF3.0 [21,22] PDF set is used to describe the dynamics of the colliding protons. Additional fixed-order predictions are generated using FEWZ [23] at $\mathcal{O}(\alpha_s^2)$ with the NNPDF3.0, CT14 [24] and MMHT14 [25] PDF sets.

3 Event selection

Events are selected containing one or two high- p_T muons produced in association with a high- p_T jet. Jets are reconstructed at LHCb using a particle flow algorithm [3] and clustered using the anti- k_T algorithm as implemented in FASTJET [26]. Additional selection requirements are placed on the jet properties in order to reduce the number of spurious jets selected. The jet energies are calibrated on an event-by-event basis. These calibrations are determined from both data and simulation, and are applied as a function of the jet p_T , azimuthal angle, pseudorapidity, charged particle fraction and the number of reconstructed PVs in the event [3]. To reduce contamination from multiple pp interactions, charged particles reconstructed within the vertex detector are only clustered into a jet if they are associated to the same PV as the final state muon(s).

The measured muons and jets are required to satisfy the fiducial requirements outlined in Sec. 1. An exception is the requirement on the p_T of the vector sum of the momentum of the muon and jet, $p_T^{\mu+j} > 20$ GeV, in Wj events. In the selection, the muon is replaced by the jet, μ -jet, which contains the signal muon after performing a jet reconstruction with relaxed jet selection requirements. The modified fiducial requirement, $p_T^{\mu\text{-jet}+j} > 20$ GeV, improves the suppression of the background from di-jets, which tend to be balanced in transverse momentum. An acceptance factor is introduced (see Sec. 5), which corrects the results to correspond to the fiducial regions defined in Sec. 1.

As Wj events contain just one final-state muon and consequently suffer from a higher background, additional requirements are placed on the sample. The background to the Wj sample from Zj events where both muons are produced in the LHCb acceptance is suppressed by rejecting events containing a second muon with p_T in excess of 20 GeV. Backgrounds from semileptonic decays of heavy-flavour hadrons are suppressed by requiring that the impact parameter of the muon track with respect to the PV should be less than 0.04 mm. Additionally, the sum of the energy associated with the track in the electromagnetic and hadronic calorimeters is required to be less than 4% of the muon momentum. In total, 8 162 Zj and 133 746 (99 683) W^+j (W^-j) candidates are selected.

4 Purity determination

The selected data samples contain background contributions from three distinct processes:

- QCD multi-jet production, which can produce muons in the final state, either due to the misidentification of hadrons, or through the semileptonic decay of heavy-flavour hadrons where a high- p_T jet is also present in the event.
- Electroweak processes, such as $Z \rightarrow \tau\tau$, $W \rightarrow \tau\nu$ or, in the case of Wj production, $Z \rightarrow \mu\mu$, can produce events that mimic the signal. Contributions are also expected from electroweak diboson and top quark production.
- A small background contribution from “fake jets” is present when the data sample contains events where the reconstructed and identified jet is not associated with

genuine particles, but is instead due to detector effects, such as the presence of fake or misreconstructed particles, or to particles produced in a different pp collision to that producing the W or Z boson.

4.1 Wj sample purity

The QCD background to the Wj sample is determined by performing an extended maximum likelihood fit to the distribution of the muon transverse momentum p_T^μ , divided by the transverse momentum of the μ -jet, $p_T^{\mu\text{-jet}}$ (where the μ -jet is defined in Sec. 3). This variable acts as a measure of muon isolation, with a value close to unity when little activity is present in the vicinity of the candidate muon and a value closer to zero as the multiplicity in the surrounding region increases. Consequently, it provides strong discrimination between muons produced in electroweak processes, which tend to be produced in isolation, and those produced in QCD processes, which are typically surrounded by additional particles. Two separate components are accounted for in the fit:

- The template shape describing all electroweak processes, including the signal, is taken from simulation. The shape of the isolation variable is approximately independent of p_T^μ , and consequently provides a good description of all electroweak processes. The simulated shape is corrected for mismodelling by applying correction factors obtained from a comparison of Zj events in data and simulation. The Wj signal contribution is subsequently separated from the other electroweak backgrounds as described below.
- The QCD background template is obtained using a di-jet enriched data sample, obtained by requiring $p_T^{\mu\text{-jet}+j} < 20$ GeV. The small contribution from signal events in the template is subtracted using simulation where the normalisation is obtained from the bin corresponding to $p_T^\mu/p_T^{\mu\text{-jet}} > 0.95$ in the signal region. The template shape is then corrected for differences in the $p_T^{\mu\text{-jet}}$ distribution between the background and signal regions.

The fits are performed in bins of η^{jet} , p_T^{jet} , and η^μ separately for positively and negatively charged Wj candidates. The background from Z decays to muons and τ leptons, where a single muon is present in the final state, is determined from simulation where the sample is normalised to the number of fully reconstructed $Z \rightarrow \mu\mu$ decays observed in data. The small contribution from WW , $t\bar{t}$ and single top events is determined using next-to-leading order (NLO) predictions obtained from MCFM [27]. Finally, the background from $W \rightarrow \tau\nu$ decays is determined by first obtaining the ratio of $W \rightarrow \tau\nu$ to $W \rightarrow \mu\nu$ events expected from simulation and normalising to the remaining signal after all other backgrounds have been determined. The background from fake jets is evaluated using simulation.

The contribution from QCD processes is found to vary between 30–70% in different bins of η^{jet} , p_T^{jet} and η^μ while the contribution from electroweak processes (including di-boson and top production) amounts to 5–10% of the selected samples. The contribution from fake jets represents approximately 0.8–0.9% of the samples. The overall purity of the W^+j

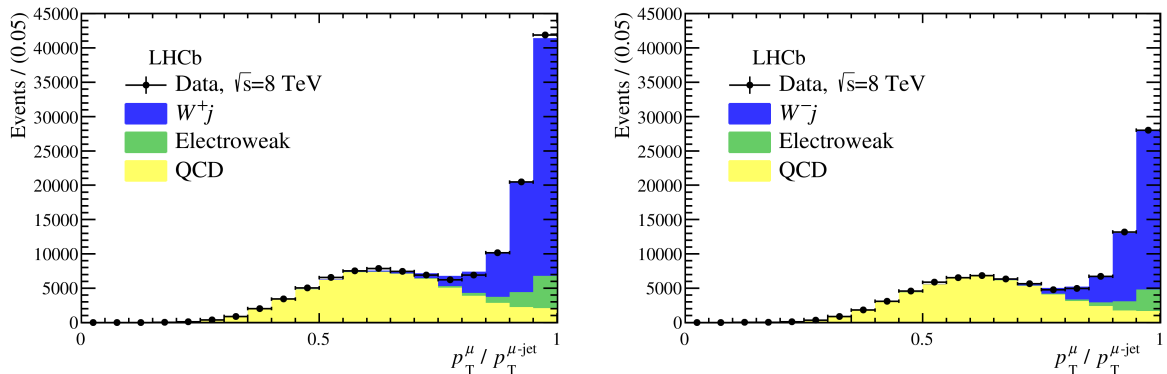


Figure 1: The contributions to the selected (left) W^+j and (right) W^-j samples are shown, where the QCD background is obtained by a fit to the $p_T^\mu/p_T^{\mu\text{-jet}}$ spectrum and the electroweak background is determined as described in the text. The contributions shown are the sum of the individual contributions in bins of η^{jet} , where the charge asymmetry typical of Wj production in pp collisions is evident.

(W^-j) sample is determined to be 46.7(36.5)% where the total contributions, obtained by summing over the yields in the η^{jet} bins, are shown in Fig. 1.

4.2 Zj sample purity

The contribution from semileptonic decays of heavy-flavour particles to the Zj sample is determined by selecting a background-enhanced sample using two approaches, where either the muons are not isolated from other activity in the event or where they do not form a good vertex. The efficiency with which the requirements select background events is evaluated by comparing the number of events selected by the two approaches as in Ref. [7]. The total contribution is estimated to be approximately 0.7%. The misidentification of hadrons as muons is evaluated as in Ref. [7], by considering the contribution from events where both muons fulfil all the selection criteria, but with both muons required to have the same sign charge; and gives a contribution of approximately 0.4%. Decays of the Z boson to τ pairs can contribute if both τ leptons subsequently decay to muons. The contribution from this source is determined from simulation to be approximately 0.1%. The number of events containing di-boson or top production is again calculated using simulation, normalised to NLO predictions from MCFM and is determined to be negligible. The contribution from fake jets is determined from simulation to amount to approximately 0.9% of the selected sample. The overall purity of the Zj sample is determined to be 97.8%.

5 Cross-section measurement

The cross-section, σ_i , for W and Z boson production in association with one or more jets in the i^{th} phase space bin is given by

$$\sigma_i = U_i \frac{\mathcal{A}_i \cdot \rho_i \cdot N_i}{\varepsilon_i^{\text{muon}} \cdot \varepsilon_i^{\text{jet}} \cdot \varepsilon_i^{\text{sel}} \cdot \mathcal{L}}, \quad (1)$$

where U_i is an unfolding correction which accounts for resolution effects causing migrations between different bins of phase space. The number of candidates selected in bin i is given by N_i while ρ_i represents the signal purity. The acceptance factor, \mathcal{A}_i , accounts for differences between the fiducial region of the measurement and the kinematic requirements placed on the muons and jets. The efficiencies for reconstructing the muons and the jet are given by $\varepsilon_i^{\text{muon}}$ and $\varepsilon_i^{\text{jet}}$, respectively, while the efficiency of any additional event selection is given by $\varepsilon_i^{\text{sel}}$.

The instantaneous luminosity is measured continuously during the acquisition of physics data by recording the rates of several selected standard processes. The effective absolute cross-section of these processes is measured during dedicated calibration periods, using both van der Meer scans [28, 29] and beam-gas imaging methods specific to the LHCb detector [30]. Both methods give consistent results and are combined to give the final luminosity calibration with an uncertainty of 1.2% [31]. The integrated luminosity of the data sample used, \mathcal{L} , is obtained from the accumulated counts of the calibrated rates and amounts to $1.98 \pm 0.02 \text{ fb}^{-1}$.

The efficiency to reconstruct and select muons in the event is evaluated using the same techniques employed in the inclusive W and Z boson measurements at LHCb [6–8]. In particular, a data-driven tag-and-probe study is performed on selected inclusive $Z \rightarrow \mu\mu$ events in data and the efficiency of reconstructing, triggering and identifying the muons is measured. These efficiencies are applied as a function of the pseudorapidity of the muon(s) in the event. The efficiency to reconstruct and identify the jet in the event $\varepsilon_i^{\text{jet}}$, is evaluated from simulation. This efficiency increases with p_{T} , from about 90% for jets with p_{T} of 20 GeV to saturate at about 95% for higher p_{T} jets. It is dominated by the probability that the jet passes the requirements designed to reject fake jets. In the case of the Wj sample, the efficiency of the additional requirements placed on the event, including a veto on extra muons, is evaluated using a “pseudo- Wj ” sample, where Zj events are selected but one muon is masked in order to mimic the neutrino in Wj events. Corrections are applied based on a comparison of the efficiency of the requirements in Wj and “pseudo- Wj ” events in simulation. The efficiency of the GEC requirement at the hardware stage of the trigger is again evaluated in a similar fashion to the inclusive analyses, where the efficiency is measured in a Zj sample selected with a looser trigger requirement [6–8]. This efficiency is evaluated separately in each kinematic bin considered in the analysis, but shows little variation with the variables that describe the jet kinematics.

The unfolding correction, U_i , corrects for differences observed in the number of events produced and measured in a given bin due to the finite resolution of the detector, where the differences are primarily caused by migrations in the $p_{\text{T}}^{\text{jet}}$ and η^{jet} distributions. The

correction is determined from simulation as the ratio of events produced in a specific bin to those recorded by the detector in the same bin. The correction varies between 0.9 and 1.0, where the largest corrections are seen at low $p_{\text{T}}^{\text{jet}}$ and in the highest and lowest η^{jet} bins.

For the Zj sample, the acceptance factor, \mathcal{A}_i , is identically equal to unity as the selection mirrors the fiducial acceptance exactly. In the case of the Wj selection, the requirement of $p_{\text{T}}^{\mu\text{-jet}+j} > 20 \text{ GeV}$ differs from the fiducial requirement of $p_{\text{T}}^{\mu+j} > 20 \text{ GeV}$. Consequently, the acceptance factor accounts for differences between these two variables arising from extra activity that may be present in the neighbourhood of the signal muon. This factor is evaluated using simulation, which is reweighted in bins of jet p_{T} and pseudorapidity to match next-to-leading order predictions obtained from aMC@NLO. The acceptance factor varies between 0.95 and 1.00 in different bins of phase space.

6 Systematic uncertainties

Several sources of systematic uncertainty have been evaluated. The uncertainty on the estimated purity of the Wj sample is evaluated by repeating the fit using alternative templates. The fit is performed for a number of different scenarios:

- the data-driven corrections are not applied to the simulated Wj shape,
- the simulated Wj shape is replaced by the “pseudo- Wj ” data sample,
- the subtraction of signal events from the background template is performed by obtaining the normalisation from simulation instead of the data-driven method outlined in Sec. 4.1.

The uncertainty on the contributions from electroweak templates is taken to be the statistical precision on the Zj and Wj samples used to perform the data-driven normalisation. For the Zj sample, the uncertainty on the misidentification background is given by the sum in quadrature of the statistical precision and the accuracy of the method, obtained by comparing the two approaches described in Sec. 4.2. This gives an uncertainty of approximately 30% on the misidentification background. The uncertainty on the contribution from semileptonic decays of heavy-flavour hadrons is about 20%, consisting of the sum in quadrature of the statistical uncertainty on the evaluated contribution, and the variation in the background level found by changing the requirements used in selecting the background-enhanced region. The uncertainty due to the presence of fake jets is taken to be the statistical uncertainty of approximately 30% on the determination of the fake-jet contribution. A similar level of agreement is observed between data and simulation by comparing kinematic distributions in regions with enhanced fake-jet populations.

The uncertainty in the muon reconstruction efficiency is determined by re-evaluating the cross-section with the total efficiency varied by one standard deviation around the central value. An additional 1% systematic uncertainty is also applied to account for differences in efficiencies observed between inclusive Z events and Zj events. The uncertainty on the

jet reconstruction efficiency is evaluated by comparing the differences in efficiency between Zj data and simulation where the quality requirements are varied about their nominal values. This results in an uncertainty of 1.9%. The uncertainty on the selection efficiency, 1%, includes the statistical uncertainty due to the limited size of the “pseudo- Wj ” data sample and the uncertainty on the corrections evaluated from simulation for differences between Wj and “pseudo- Wj ” events. The uncertainty on the GEC efficiency is taken to be the sum in quadrature of the accuracy of the method, 0.3% [7, 8], and the difference observed between W^+j , W^-j and Zj events in simulation, typically smaller than 0.2%. The uncertainty on the efficiency with which jets are selected is evaluated by varying the selection requirements and determining how the fraction of events rejected agrees between data and simulation, using the methods described in Ref. [3]. Agreement is typically seen at the level of about 1.7%. This is taken as an uncertainty on the modelling of the efficiencies in simulation, and is combined in quadrature with the statistical precision with which the efficiencies are determined.

The uncertainty on the acceptance factor, \mathcal{A}_i , is determined by comparing the values obtained with and without NLO reweighting performed, and by comparing the acceptance calculated in “pseudo- Wj ” events in data and simulation. These individual differences, contributing 0.5% and 0.3%, respectively, are added in quadrature with the statistical precision of the determination.

Two contributions to the uncertainty on the unfolding correction, U_i , are considered. The variation of the corrections is evaluated by comparing the difference in the number of Zj events between the bin-by-bin corrections employed in the analysis and a Bayesian unfolding [32, 33] with two iterations. The difference is typically 0.8–1.5%, depending on the distribution considered. This is larger than the variation seen when changing the number of iterations in the Bayesian approach, and it is also larger than the effect of reweighting the bin-by-bin corrections to the jet transverse momentum distributions produced by different event generators. An additional uncertainty due to the resolution of the jet pseudorapidity in data is also considered and obtained by comparing the difference between the jet pseudorapidity calculated using just the charged component of the jet and using both the charged and neutral components in Zj data and simulation. A good level of agreement is observed within the statistical precision of 0.5%. The two contributions are added in quadrature and taken as the systematic uncertainty associated with the unfolding corrections.

Different sources for the jet energy scale uncertainty are considered. The energy scale associated with tracks is known and simulated to an accuracy of better than 1% [12]. The calorimeter energy scales are modelled to an accuracy of better than 10%. This is confirmed by comparing the fraction of p_T^{jet} carried by neutral final-state particles between data and simulation, and evaluating how much the calorimeter response can be varied before disagreement is observed. The jet energy resolution at LHCb is modelled in simulation to an accuracy of about 10% [3, 5]. The analysis is repeated with the simulated p_T^{jet} smeared by 10%; the change in the final result of approximately 0.3% is assigned as the relevant uncertainty. Combining these effects yields an energy scale uncertainty of about 3%, consistent with previous studies [3] considering the p_T balance in $Z + 1$ -jet events. In

order to determine the effect on the measurement, the analysis is repeated with the energy scale varied to cover possible differences between data and simulation. The variation in the measured cross-sections lies between 4 and 11%, depending on the bin and sample considered. This is assigned as the energy scale uncertainty.

A summary of the different contributions to the systematic and total uncertainty for the measured quantities which will be outlined in Sec. 7 is given in Table 1. In the case of Zj measurements, the systematic uncertainty is dominated by the knowledge of the jet energy scale, while for Wj measurements a similarly large uncertainty is present due to the determination of the sample purity.

7 Results

The total cross-sections for Wj and Zj production are obtained by summing over the measured cross-sections in bins of η^{jet} . All statistical uncertainties are taken to be uncorrelated, while uncertainties arising from common sources and/or methods are taken to be fully correlated between different bins. The cross-sections are calculated to be

$$\begin{aligned}\sigma_{W^+j} &= 56.9 \pm 0.2 \pm 5.1 \pm 0.7 \text{ pb}, \\ \sigma_{W^-j} &= 33.1 \pm 0.2 \pm 3.5 \pm 0.4 \text{ pb}, \\ \sigma_{Zj} &= 5.71 \pm 0.06 \pm 0.27 \pm 0.07 \text{ pb},\end{aligned}$$

where the first uncertainties are statistical, the second are systematic, and the third are due to the luminosity determination. The ratios of Wj and Zj production are determined to be

$$\begin{aligned}R_{WZ} &= 15.8 \pm 0.2 \pm 1.1, \\ R_{W^+Z} &= 10.0 \pm 0.1 \pm 0.6, \\ R_{W^-Z} &= 5.8 \pm 0.1 \pm 0.5, \\ R_{W^\pm} &= 1.72 \pm 0.01 \pm 0.06,\end{aligned}$$

where R_{WZ} , R_{W^+Z} and R_{W^-Z} represent, respectively, the ratio of the Wj , W^+j and W^-j cross-sections to the Zj cross-section, and R_{W^\pm} represents the ratio of the W^+j to W^-j cross-sections. The asymmetry of W^+j and W^-j production, $A(Wj)$, is given by

$$A(Wj) \equiv (\sigma_{W^+j} - \sigma_{W^-j}) / (\sigma_{W^+j} + \sigma_{W^-j}) = 0.264 \pm 0.003 \pm 0.015.$$

In the above results, the first uncertainties are statistical and the second are systematic.

The results are compared to theoretical predictions calculated using the aMC@NLO and POWHEG generators in Fig. 2. The uncertainty on the theoretical predictions due to higher-order effects is calculated by varying the renormalisation and factorisation scales independently by a factor of two around the nominal scale [34]. Additional uncertainties arise from the description of the PDFs, and the value of the strong coupling, α_s . The total theoretical uncertainty is obtained by combining the PDF and α_s uncertainties in

Table 1: Summary of the different contributions to the total uncertainty on σ_{W+j} , σ_{W-j} , σ_{Zj} and their ratios given as a percentage of the measured observable.

Source	σ_{W+j}	σ_{W-j}	σ_{Zj}	R_{WZ}	$R_{W\pm}$
Statistical	0.4	0.5	1.1	1.2	0.7
Muon reconstruction	1.3	1.3	0.6	0.9	0.0
Jet reconstruction	1.9	1.9	1.9	0.0	0.0
Selection	1.0	1.0	0.0	1.0	0.0
GEC	0.5	0.5	0.4	0.2	0.1
Purity	5.5	7.0	0.4	6.0	2.5
Acceptance	0.6	0.6	0.0	0.6	0.0
Unfolding	0.8	0.8	0.8	0.0	0.2
Jet energy	6.5	7.7	4.3	3.4	1.2
Total Systematic	8.9	10.7	4.8	7.0	3.3
Luminosity	1.2	1.2	1.2	–	–

quadrature, and adding the result to the scale uncertainty linearly. The measurements are represented by bands where the inner band represents the statistical uncertainty and the outer band the total uncertainty. In the cross-section measurements, the scale uncertainty dominates the theoretical uncertainty, while it largely cancels in the ratios and asymmetry. The data and predictions are further compared differentially for Wj production in Figs. 3 and 4, and for Zj production in Figs. 5 and 6, with good agreement seen in all distributions.

Further to the total and differential production cross-sections, measurements of the charge ratio and asymmetry of Wj production are also performed as a function of lepton pseudorapidity and are compared to POWHEG and aMC@NLO in Fig. 7. Due to the cancellation of scale uncertainties, these distributions are expected to show sensitivity to the PDFs and consequently are also compared in Fig. 8 to fixed-order calculations performed with FEWZ separately for the NNPDF3.0, CT14 and MMHT14 PDF sets. The fixed-order predictions are expected to give a good description of the ratios and asymmetries as the effects of higher-order terms and hadronisation largely cancel between the positively and negatively charged Wj predictions. In general, good agreement is seen between the data and the predictions, although the data presents a slightly larger ratio and asymmetry, particularly in the first bin of η^μ . However, when the spread of predictions obtained using different PDF sets is considered, the deviations are not significant.

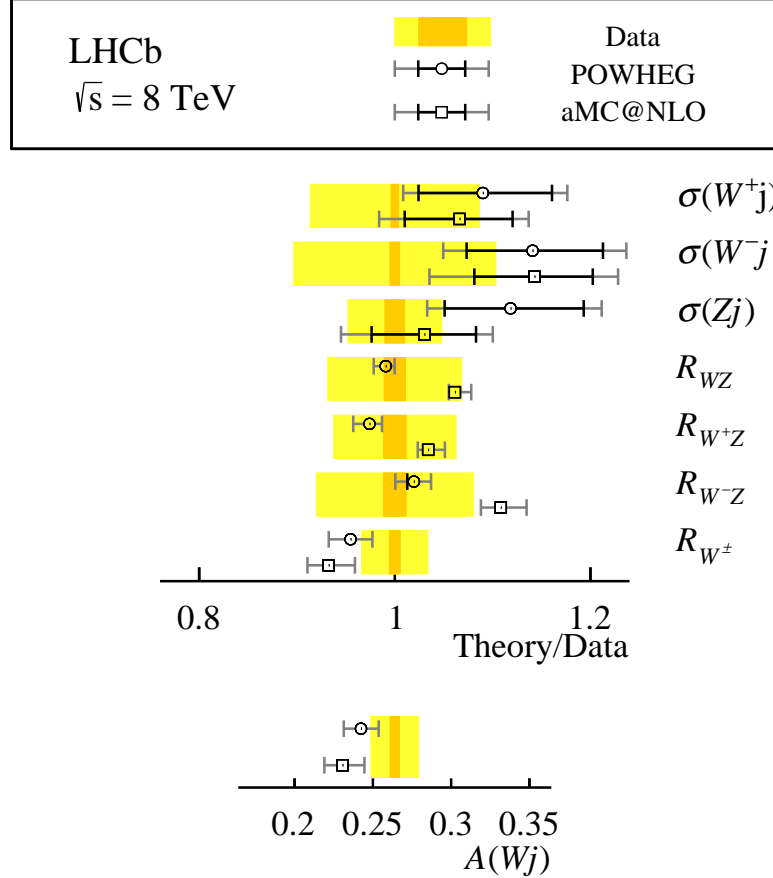


Figure 2: Summary of the measurements performed in the fiducial region, as defined in Sec. 1. The measurements are shown as bands, while the theoretical predictions are presented as points. For the experimental measurements, the inner band represents the statistical uncertainty, while the outer band represents the total uncertainty. For the theory points, the inner error bar represents the scale uncertainty, while the outer bar represents the total uncertainty. The cross-sections and ratios are shown normalised to the measurement, while the asymmetry is presented separately.

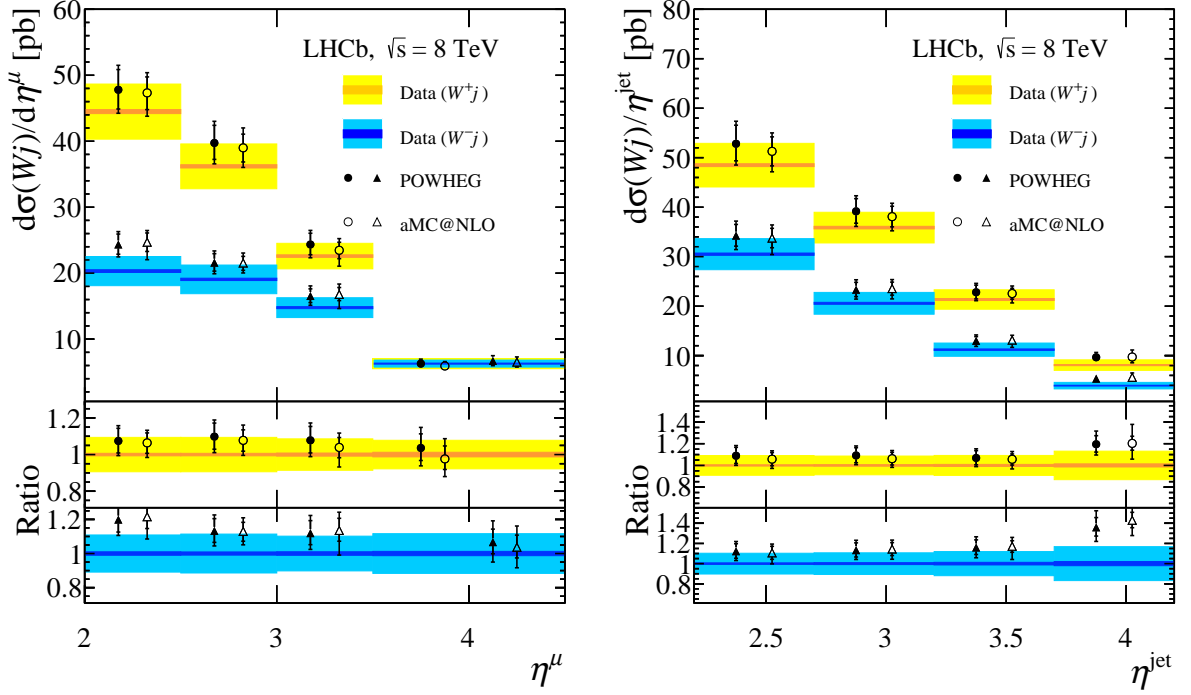


Figure 3: Wj bin-averaged differential cross-sections as a function of η^μ (left) and η^{jet} (right). The measurements are shown as bands representing the statistical and total uncertainties, while the theoretical predictions are shown as points (displaced horizontally for presentation) representing the same bin-averaged cross-sections as the data. The inner error bar represents the scale uncertainty, and the outer error bar represents the total uncertainty. The ratio of the predicted to measured cross-sections is shown below the distribution. The W^+j and W^-j cross-sections are seen to overlap in the final bin in η^μ .

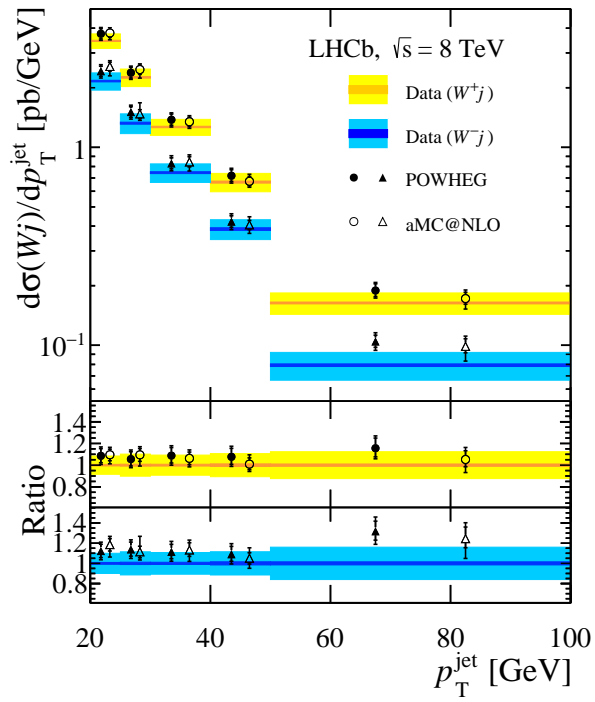


Figure 4: Wj bin-averaged differential cross-sections as a function of p_T^{jet} . The experimental and theoretical components are shown as in Fig. 3. The ratio of the predicted to measured cross-sections is shown below the distribution.

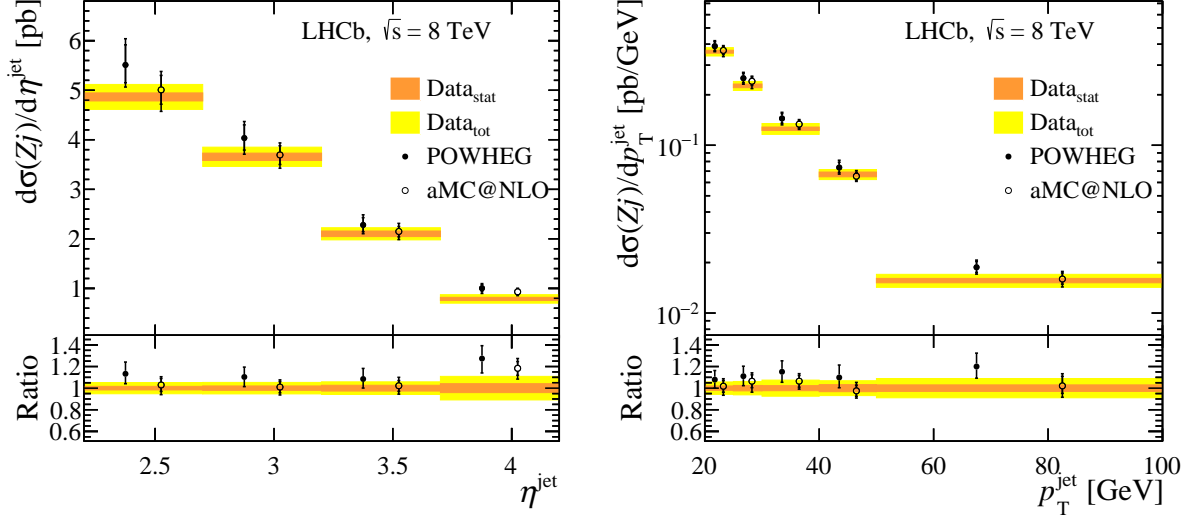


Figure 5: The measured bin-averaged differential Zj production cross-section is shown as a function of (left) η^{jet} and (right) p_T^{jet} . The experimental measurements are shown as bands, while the theoretical predictions are shown as points, horizontally displaced for presentation. The ratio of the predicted to measured cross-sections is shown below the distribution.

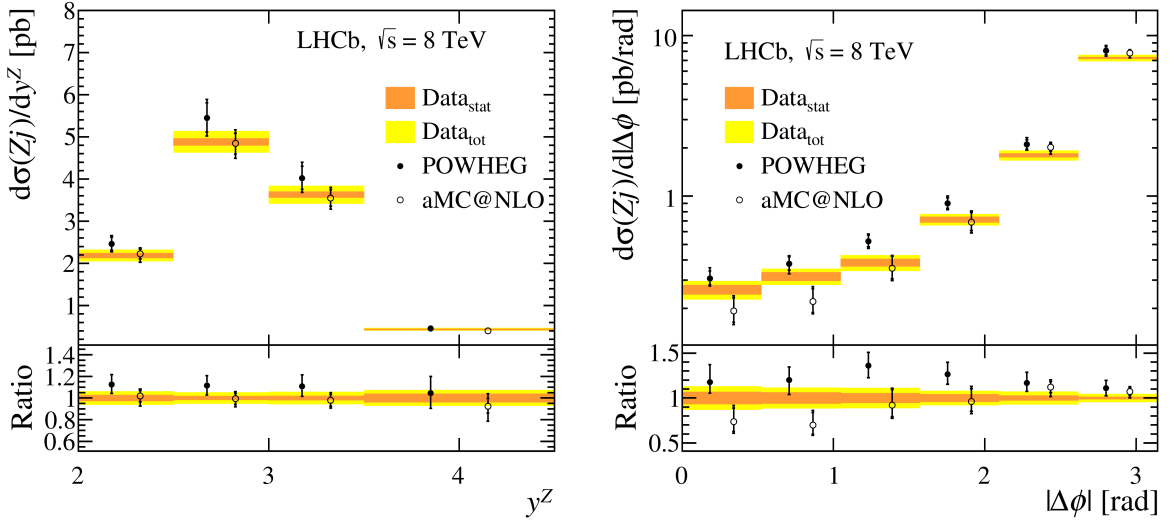


Figure 6: The measured bin-averaged differential Zj production cross-section is shown as a function of (left) y^Z and (right) azimuthal separation between the Z boson and the jet. The experimental measurements are shown as bands, while the theoretical predictions are shown as points, horizontally displaced for presentation. The ratio of the predicted to measured cross-sections is shown below the distribution.

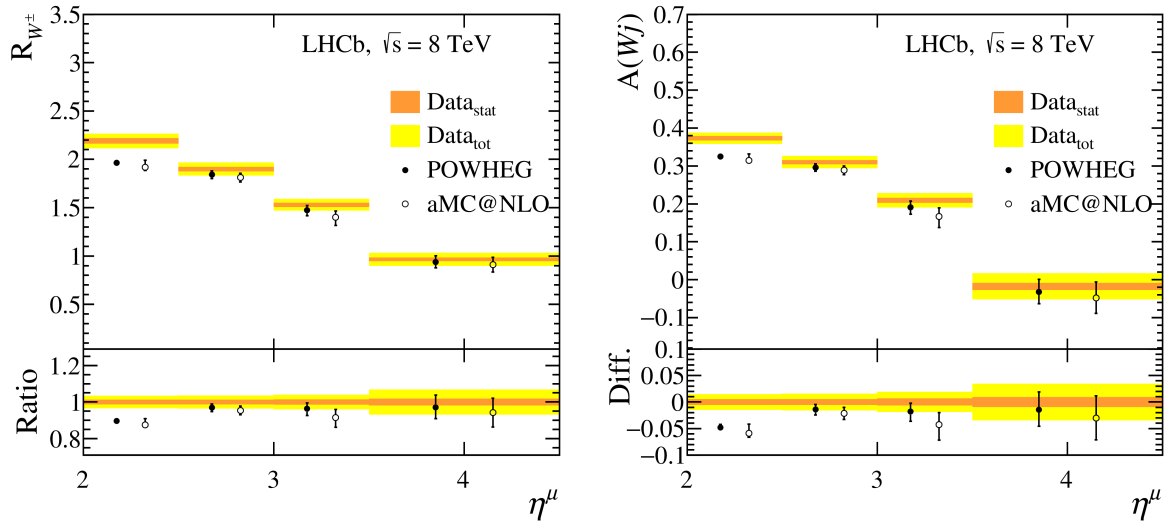


Figure 7: Ratio (left) and asymmetry (right) of W^+j to W^-j production as a function of the lepton pseudorapidity. The experimental measurements are shown as bands, while the theoretical predictions are shown as points, horizontally displaced for presentation. The ratio of the predictions to the experimentally measured values is shown below the distribution for the charge ratio, while their difference is shown for the charge asymmetry.

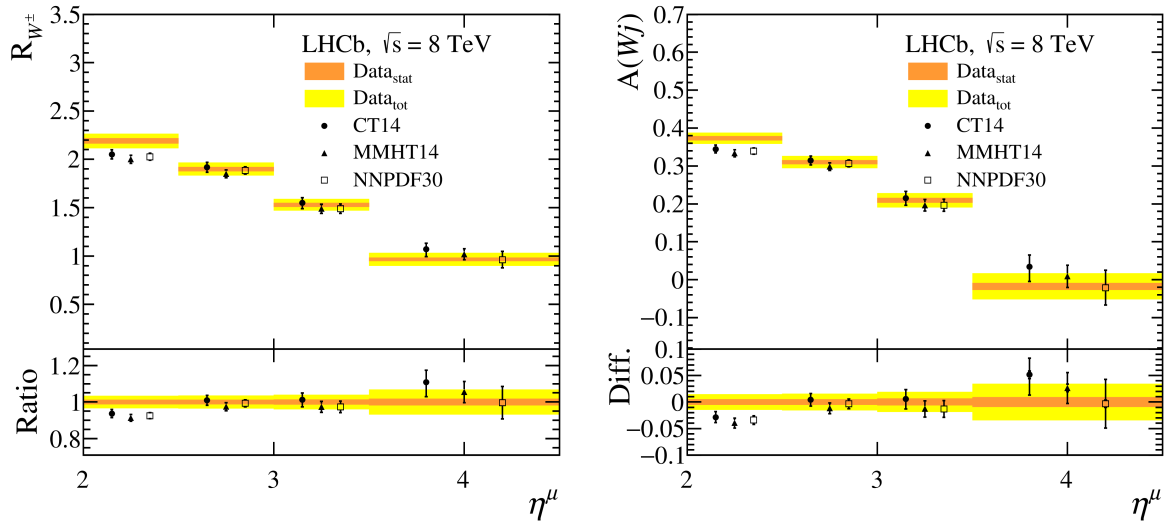


Figure 8: Ratio (left) and asymmetry (right) of W^+j to W^-j production as a function of the lepton pseudorapidity compared to NLO calculations performed with the FEWZ generator and three different PDF sets. The experimental measurements are shown as bands, while the theoretical predictions are shown as points, horizontally displaced for presentation. The same comparisons are shown below the distribution as described in Fig. 7.

8 Conclusions

Measurements of the forward W and Z boson cross-sections in association with jets at $\sqrt{s} = 8$ TeV are presented. The W bosons are reconstructed in the decay $W \rightarrow \mu\nu_\mu$ and the Z bosons in the decay $Z \rightarrow \mu\mu$. Total cross-sections are presented in the forward fiducial region in addition to measurements of the charge ratio and asymmetry of Wj production and the ratio of Wj to Zj production. Differential cross-sections are presented as a function of p_T^{jet} , η^{jet} , η^μ in the case of Wj production, and for Zj production, where a full reconstruction of the final state is possible, measurements are presented as a function of p_T^{jet} , η^{jet} , y^Z , and the azimuthal separation of the Z boson and the jet, $|\Delta\phi|$. The Wj charge ratio and asymmetry are presented as a function of η^μ . All measurements are observed to be in agreement with predictions obtained at $\mathcal{O}(\alpha_s^2)$ interfaced with a parton shower in order to achieve NLO plus leading-log accuracy. The measurements of the charge ratio and asymmetry of Wj production are also compared to predictions obtained at $\mathcal{O}(\alpha_s^2)$ in fixed order perturbative QCD and show good agreement.

Acknowledgements

We express our gratitude to our colleagues in the CERN accelerator departments for the excellent performance of the LHC. We thank the technical and administrative staff at the LHCb institutes. We acknowledge support from CERN and from the national agencies: CAPES, CNPq, FAPERJ and FINEP (Brazil); NSFC (China); CNRS/IN2P3 (France); BMBF, DFG and MPG (Germany); INFN (Italy); FOM and NWO (The Netherlands); MNiSW and NCN (Poland); MEN/IFA (Romania); MinES and FANO (Russia); MinECo (Spain); SNSF and SER (Switzerland); NASU (Ukraine); STFC (United Kingdom); NSF (USA). We acknowledge the computing resources that are provided by CERN, IN2P3 (France), KIT and DESY (Germany), INFN (Italy), SURF (The Netherlands), PIC (Spain), GridPP (United Kingdom), RRCKI and Yandex LLC (Russia), CSCS (Switzerland), IFIN-HH (Romania), CBPF (Brazil), PL-GRID (Poland) and OSC (USA). We are indebted to the communities behind the multiple open source software packages on which we depend. Individual groups or members have received support from AvH Foundation (Germany), EPLANET, Marie Skłodowska-Curie Actions and ERC (European Union), Conseil Général de Haute-Savoie, Labex ENIGMASS and OCEVU, Région Auvergne (France), RFBR and Yandex LLC (Russia), GVA, XuntaGal and GENCAT (Spain), Herchel Smith Fund, The Royal Society, Royal Commission for the Exhibition of 1851 and the Leverhulme Trust (United Kingdom).

References

- [1] R. S. Thorne, A. D. Martin, W. J. Stirling, and G. Watt, *Parton distributions and QCD at LHCb*, in *Proceedings, 16th International Workshop on Deep Inelastic Scattering and Related Subjects (DIS 2008)*, p. 30, 2008. [arXiv:0808.1847](#). doi: 10.3360/dis.2008.30.
- [2] S. Farry and R. Gauld, *Leptonic W^\pm boson asymmetry in association with jets at LHCb and parton distribution function constraints at large x* , *Phys. Rev.* **D93** (2016) 014008, [arXiv:1505.01399](#).
- [3] LHCb collaboration, R. Aaij *et al.*, *Study of forward Z +jet production in pp collisions at $\sqrt{s} = 7$ TeV*, *JHEP* **01** (2014) 033, [arXiv:1310.8197](#).
- [4] LHCb collaboration, R. Aaij *et al.*, *Measurement of the Z + b -jet cross-section in pp collisions at $\sqrt{s} = 7$ TeV in the forward region*, *JHEP* **01** (2015) 064, [arXiv:1411.1264](#).
- [5] LHCb collaboration, R. Aaij *et al.*, *Study of W boson production in association with beauty and charm*, *Phys. Rev.* **D92** (2015) 052012, [arXiv:1505.04051](#).
- [6] LHCb collaboration, R. Aaij *et al.*, *Measurement of the forward W boson production cross-section in pp collisions at $\sqrt{s} = 7$ TeV*, *JHEP* **12** (2014) 079, [arXiv:1408.4354](#).

- [7] LHCb collaboration, R. Aaij *et al.*, *Measurement of the forward Z boson cross-section in pp collisions at $\sqrt{s} = 7$ TeV*, JHEP **08** (2015) 039, [arXiv:1505.07024](#).
- [8] LHCb collaboration, R. Aaij *et al.*, *Measurement of forward W and Z boson production in pp collisions at $\sqrt{s} = 8$ TeV*, JHEP **01** (2015) 155, [arXiv:1511.08039](#).
- [9] M. Cacciari, G. P. Salam, and G. Soyez, *The anti- k_t jet clustering algorithm*, JHEP **04** (2008) 063, [arXiv:0802.1189](#).
- [10] S. Alioli, P. Nason, C. Oleari, and E. Re, *A general framework for implementing NLO calculations in shower Monte Carlo programs: The POWHEG BOX*, JHEP **06** (2010) 043, [arXiv:1002.2581](#).
- [11] LHCb collaboration, A. A. Alves Jr. *et al.*, *The LHCb detector at the LHC*, JINST **3** (2008) S08005.
- [12] LHCb collaboration, R. Aaij *et al.*, *LHCb detector performance*, Int. J. Mod. Phys. **A30** (2015) 1530022, [arXiv:1412.6352](#).
- [13] T. Sjöstrand, S. Mrenna, and P. Skands, *A brief introduction to PYTHIA 8.1*, Comput. Phys. Commun. **178** (2008) 852, [arXiv:0710.3820](#); T. Sjöstrand, S. Mrenna, and P. Skands, *PYTHIA 6.4 physics and manual*, JHEP **05** (2006) 026, [arXiv:hep-ph/0603175](#).
- [14] I. Belyaev *et al.*, *Handling of the generation of primary events in Gauss, the LHCb simulation framework*, J. Phys. Conf. Ser. **331** (2011) 032047.
- [15] D. J. Lange, *The EvtGen particle decay simulation package*, Nucl. Instrum. Meth. **A462** (2001) 152.
- [16] P. Golonka and Z. Was, *PHOTOS Monte Carlo: A precision tool for QED corrections in Z and W decays*, Eur. Phys. J. **C45** (2006) 97, [arXiv:hep-ph/0506026](#).
- [17] Geant4 collaboration, J. Allison *et al.*, *Geant4 developments and applications*, IEEE Trans. Nucl. Sci. **53** (2006) 270; Geant4 collaboration, S. Agostinelli *et al.*, *Geant4: A simulation toolkit*, Nucl. Instrum. Meth. **A506** (2003) 250.
- [18] M. Clemencic *et al.*, *The LHCb simulation application, Gauss: Design, evolution and experience*, J. Phys. Conf. Ser. **331** (2011) 032023.
- [19] S. Alioli, P. Nason, C. Oleari, and E. Re, *Vector boson plus one jet production in POWHEG*, JHEP **01** (2011) 095, [arXiv:1009.5594](#).
- [20] J. Alwall *et al.*, *The automated computation of tree-level and next-to-leading order differential cross sections, and their matching to parton shower simulations*, JHEP **07** (2014) 079, [arXiv:1405.0301](#).

- [21] R. D. Ball *et al.*, *A first unbiased global NLO determination of parton distributions and their uncertainties*, Nucl. Phys. **B838** (2010) 136, [arXiv:1002.4407](#).
- [22] NNPDF, R. D. Ball *et al.*, *Parton distributions for the LHC Run II*, JHEP **04** (2015) 040, [arXiv:1410.8849](#).
- [23] R. Gavin, Y. Li, F. Petriello, and S. Quackenbush, *FEWZ 2.0: A code for hadronic Z production at next-to-next-to-leading order*, Comput. Phys. Commun. **182** (2011) 2388, [arXiv:1011.3540](#).
- [24] S. Dulat *et al.*, *New parton distribution functions from a global analysis of quantum chromodynamics*, Phys. Rev. **D93** (2016) 033006, [arXiv:1506.07443](#).
- [25] L. A. Harland-Lang, A. D. Martin, P. Motylinski, and R. S. Thorne, *Parton distributions in the LHC era: MMHT 2014 PDFs*, Eur. Phys. J. **C75** (2015) 204, [arXiv:1412.3989](#).
- [26] M. Cacciari and G. P. Salam, *Dispelling the N^3 myth for the k_t jet-finder*, Phys. Lett. **B641** (2006) 57, [arXiv:hep-ph/0512210](#).
- [27] J. M. Campbell and R. K. Ellis, *Radiative corrections to $Zb\bar{b}$ production*, Phys. Rev. **D62** (2000) 114012, [arXiv:hep-ph/0006304](#).
- [28] S. van der Meer, *Calibration of the effective beam height in the ISR*, CERN-ISR-PO-68-31 (1968).
- [29] C. Barschel, *Precision luminosity measurement at LHCb with beam-gas imaging*, PhD thesis, RWTH Aachen U., 2014, Presented 05 Mar 2014, <https://cds.cern.ch/record/1693671>.
- [30] M. Ferro-Luzzi, *Proposal for an absolute luminosity determination in colliding beam experiments using vertex detection of beam-gas interactions*, Nucl. Instrum. Meth. **A553** (2005) 388.
- [31] LHCb collaboration, R. Aaij *et al.*, *Precision luminosity measurements at LHCb*, JINST **9** (2014) P12005, [arXiv:1410.0149](#).
- [32] G. D'Agostini, *A multidimensional unfolding method based on Bayes' theorem*, Nucl. Instrum. Meth. **A362** (1995) 487.
- [33] T. Auye, *Unfolding algorithms and tests using RooUnfold*, in *Proceedings of the PHYSTAT 2011 Workshop, CERN, Geneva, Switzerland, January 2011, CERN-2011-006*, pp. 313–318, 2011. [arXiv:1105.1160](#).
- [34] K. Hamilton, P. Nason, E. Re, and G. Zanderighi, *NNLOPS simulation of Higgs boson production*, JHEP **10** (2013) 222, [arXiv:1309.0017](#).

LHCb collaboration

R. Aaij³⁹, C. Abellán Beteta⁴¹, B. Adeva³⁸, M. Adinolfi⁴⁷, Z. Ajaltouni⁵, S. Akar⁶, J. Albrecht¹⁰, F. Alessio³⁹, M. Alexander⁵², S. Ali⁴², G. Alkhazov³¹, P. Alvarez Cartelle⁵⁴, A.A. Alves Jr⁵⁸, S. Amato², S. Amerio²³, Y. Amhis⁷, L. An⁴⁰, L. Anderlini¹⁸, G. Andreassi⁴⁰, M. Andreotti^{17,g}, J.E. Andrews⁵⁹, R.B. Appleby⁵⁵, O. Aquines Gutierrez¹¹, F. Archilli¹, P. d'Argent¹², J. Arnau Romeu⁶, A. Artamonov³⁶, M. Artuso⁶⁰, E. Aslanides⁶, G. Auriemma^{26,s}, M. Baalouch⁵, S. Bachmann¹², J.J. Back⁴⁹, A. Badalov³⁷, C. Baesso⁶¹, W. Baldini¹⁷, R.J. Barlow⁵⁵, C. Barschel³⁹, S. Barsuk⁷, W. Barter³⁹, V. Batozskaya²⁹, V. Battista⁴⁰, A. Bay⁴⁰, L. Beaucourt⁴, J. Beddow⁵², F. Bedeschi²⁴, I. Bediaga¹, L.J. Bel⁴², V. Bellee⁴⁰, N. Belloli^{21,i}, K. Belous³⁶, I. Belyaev³², E. Ben-Haim⁸, G. Bencivenni¹⁹, S. Benson³⁹, J. Benton⁴⁷, A. Berezhnoy³³, R. Bernet⁴¹, A. Bertolin²³, M.-O. Bettler³⁹, M. van Beuzekom⁴², S. Bifani⁴⁶, P. Billoir⁸, T. Bird⁵⁵, A. Birnkraut¹⁰, A. Bitadze⁵⁵, A. Bizzeti^{18,u}, T. Blake⁴⁹, F. Blanc⁴⁰, J. Blouw¹¹, S. Blusk⁶⁰, V. Bocci²⁶, T. Boettcher⁵⁷, A. Bondar³⁵, N. Bondar^{31,39}, W. Bonivento¹⁶, S. Borghi⁵⁵, M. Borisyak⁶⁷, M. Borsato³⁸, F. Bossu⁷, M. Boubdir⁹, T.J.V. Bowcock⁵³, E. Bowen⁴¹, C. Bozzi^{17,39}, S. Braun¹², M. Britsch¹², T. Britton⁶⁰, J. Brodzicka⁵⁵, E. Buchanan⁴⁷, C. Burr⁵⁵, A. Bursche², J. Buytaert³⁹, S. Cadeddu¹⁶, R. Calabrese^{17,g}, M. Calvi^{21,i}, M. Calvo Gomez^{37,m}, P. Campana¹⁹, D. Campora Perez³⁹, L. Capriotti⁵⁵, A. Carbone^{15,e}, G. Carboni^{25,j}, R. Cardinale^{20,h}, A. Cardini¹⁶, P. Carniti^{21,i}, L. Carson⁵¹, K. Carvalho Akiba², G. Casse⁵³, L. Cassina^{21,i}, L. Castillo Garcia⁴⁰, M. Cattaneo³⁹, Ch. Cauet¹⁰, G. Cavallero²⁰, R. Cenci^{24,t}, M. Charles⁸, Ph. Charpentier³⁹, G. Chatzikonstantinidis⁴⁶, M. Chefdeville⁴, S. Chen⁵⁵, S.-F. Cheung⁵⁶, V. Chobanova³⁸, M. Chrzaszcz^{41,27}, X. Cid Vidal³⁸, G. Ciezarek⁴², P.E.L. Clarke⁵¹, M. Clemencic³⁹, H.V. Cliff⁴⁸, J. Closier³⁹, V. Coco⁵⁸, J. Cogan⁶, E. Cogneras⁵, V. Cogoni^{16,f}, L. Cojocariu³⁰, G. Collazuol^{23,o}, P. Collins³⁹, A. Comerma-Montells¹², A. Contu³⁹, A. Cook⁴⁷, S. Coquereau⁸, G. Corti³⁹, M. Corvo^{17,g}, C.M. Costa Sobral⁴⁹, B. Couturier³⁹, G.A. Cowan⁵¹, D.C. Craik⁵¹, A. Crocombe⁴⁹, M. Cruz Torres⁶¹, S. Cunliffe⁵⁴, R. Currie⁵⁴, C. D'Ambrosio³⁹, E. Dall'Occo⁴², J. Dalseno⁴⁷, P.N.Y. David⁴², A. Davis⁵⁸, O. De Aguiar Francisco², K. De Bruyn⁶, S. De Capua⁵⁵, M. De Cian¹², J.M. De Miranda¹, L. De Paula², P. De Simone¹⁹, C.-T. Dean⁵², D. Decamp⁴, M. Deckenhoff¹⁰, L. Del Buono⁸, M. Demmer¹⁰, D. Derkach⁶⁷, O. Deschamps⁵, F. Dettori³⁹, B. Dey²², A. Di Canto³⁹, H. Dijkstra³⁹, F. Dordei³⁹, M. Dorigo⁴⁰, A. Dosil Suárez³⁸, A. Dovbnya⁴⁴, K. Dreimanis⁵³, L. Dufour⁴², G. Dujany⁵⁵, K. Dungs³⁹, P. Durante³⁹, R. Dzhelyadin³⁶, A. Dziurda³⁹, A. Dzyuba³¹, N. Déleage⁴, S. Easo⁵⁰, U. Egede⁵⁴, V. Egorychev³², S. Eidelman³⁵, S. Eisenhardt⁵¹, U. Eitschberger¹⁰, R. Ekelhof¹⁰, L. Eklund⁵², Ch. Elsasser⁴¹, S. Ely⁶⁰, S. Esen¹², H.M. Evans⁴⁸, T. Evans⁵⁶, A. Falabella¹⁵, N. Farley⁴⁶, S. Farry⁵³, R. Fay⁵³, D. Ferguson⁵¹, V. Fernandez Albor³⁸, F. Ferrari^{15,39}, F. Ferreira Rodrigues¹, M. Ferro-Luzzi³⁹, S. Filippov³⁴, M. Fiore^{17,g}, M. Fiorini^{17,g}, M. Firlej²⁸, C. Fitzpatrick⁴⁰, T. Fiutowski²⁸, F. Fleuret^{7,b}, K. Fohl³⁹, M. Fontana¹⁶, F. Fontanelli^{20,h}, D.C. Forshaw⁶⁰, R. Forty³⁹, M. Frank³⁹, C. Frei³⁹, M. Frosini¹⁸, J. Fu^{22,q}, E. Furfaro^{25,j}, C. Färber³⁹, A. Gallas Torreira³⁸, D. Galli^{15,e}, S. Gallorini²³, S. Gambetta⁵¹, M. Gandelman², P. Gandini⁵⁶, Y. Gao³, J. García Pardiñas³⁸, J. Garra Tico⁴⁸, L. Garrido³⁷, P.J. Garsed⁴⁸, D. Gascon³⁷, C. Gaspar³⁹, L. Gavardi¹⁰, G. Gazzoni⁵, D. Gerick¹², E. Gersabeck¹², M. Gersabeck⁵⁵, T. Gershon⁴⁹, Ph. Ghez⁴, S. Gianì⁴⁰, V. Gibson⁴⁸, O.G. Girard⁴⁰, L. Giubega³⁰, K. Gizdov⁵¹, V.V. Gligorov⁸, D. Golubkov³², A. Golutvin^{54,39}, A. Gomes^{1,a}, I.V. Gorelov³³, C. Gotti^{21,i}, M. Grabalosa Gándara⁵, R. Graciani Diaz³⁷, L.A. Granado Cardoso³⁹, E. Graugés³⁷, E. Graverini⁴¹, G. Graziani¹⁸, A. Greco³⁰, P. Griffith⁴⁶, L. Grillo¹², B.R. Gruberg Cazon⁵⁶, O. Grünberg⁶⁵, E. Gushchin³⁴,

Yu. Guz³⁶, T. Gys³⁹, C. Göbel⁶¹, T. Hadavizadeh⁵⁶, C. Hadjivasiliou⁶⁰, G. Haefeli⁴⁰, C. Haen³⁹,
 S.C. Haines⁴⁸, S. Hall⁵⁴, B. Hamilton⁵⁹, X. Han¹², S. Hansmann-Menzemer¹², N. Harnew⁵⁶,
 S.T. Harnew⁴⁷, J. Harrison⁵⁵, J. He³⁹, T. Head⁴⁰, A. Heister⁹, K. Hennessy⁵³, P. Henrard⁵,
 L. Henry⁸, J.A. Hernando Morata³⁸, E. van Herwijnen³⁹, M. Heß⁶⁵, A. Hicheur², D. Hill⁵⁶,
 C. Hombach⁵⁵, W. Hulsbergen⁴², T. Humair⁵⁴, M. Hushchyn⁶⁷, N. Hussain⁵⁶, D. Hutchcroft⁵³,
 M. Idzik²⁸, P. Ilten⁵⁷, R. Jacobsson³⁹, A. Jaeger¹², J. Jalocha⁵⁶, E. Jans⁴², A. Jawahery⁵⁹,
 M. John⁵⁶, D. Johnson³⁹, C.R. Jones⁴⁸, C. Joram³⁹, B. Jost³⁹, N. Jurik⁶⁰, S. Kandybei⁴⁴,
 W. Kanso⁶, M. Karacson³⁹, J.M. Kariuki⁴⁷, S. Karodia⁵², M. Kecke¹², M. Kelsey⁶⁰,
 I.R. Kenyon⁴⁶, M. Kenzie³⁹, T. Ketel⁴³, E. Khairullin⁶⁷, B. Khanji^{21,39,i}, C. Khurewathanakul⁴⁰,
 T. Kirn⁹, S. Klaver⁵⁵, K. Klimaszewski²⁹, S. Koliiev⁴⁵, M. Kolpin¹², I. Komarov⁴⁰,
 R.F. Koopman⁴³, P. Koppenburg⁴², A. Kozachuk³³, M. Kozeiha⁵, L. Kravchuk³⁴, K. Kreplin¹²,
 M. Kreps⁴⁹, P. Krokovny³⁵, F. Kruse¹⁰, W. Krzemien²⁹, W. Kucewicz^{27,l}, M. Kucharczyk²⁷,
 V. Kudryavtsev³⁵, A.K. Kuonen⁴⁰, K. Kurek²⁹, T. Kvaratskheliya^{32,39}, D. Lacarrere³⁹,
 G. Lafferty^{55,39}, A. Lai¹⁶, D. Lambert⁵¹, G. Lanfranchi¹⁹, C. Langenbruch⁴⁹, B. Langhans³⁹,
 T. Latham⁴⁹, C. Lazzeroni⁴⁶, R. Le Gac⁶, J. van Leerdam⁴², J.-P. Lees⁴, A. Leflat^{33,39},
 J. Lefrançois⁷, R. Lefèvre⁵, F. Lemaitre³⁹, E. Lemos Cid³⁸, O. Leroy⁶, T. Lesiak²⁷,
 B. Leverington¹², Y. Li⁷, T. Likhomanenko^{67,66}, R. Lindner³⁹, C. Linn³⁹, F. Lionetto⁴¹,
 B. Liu¹⁶, X. Liu³, D. Loh⁴⁹, I. Longstaff⁵², J.H. Lopes², D. Lucchesi^{23,o}, M. Lucio Martinez³⁸,
 H. Luo⁵¹, A. Lupato²³, E. Luppi^{17,g}, O. Lupton⁵⁶, A. Lusiani²⁴, X. Lyu⁶², F. Machefert⁷,
 F. Maciuc³⁰, O. Maev³¹, K. Maguire⁵⁵, S. Malde⁵⁶, A. Malinin⁶⁶, T. Maltsev³⁵, G. Manca⁷,
 G. Mancinelli⁶, P. Manning⁶⁰, J. Maratas⁵, J.F. Marchand⁴, U. Marconi¹⁵, C. Marin Benito³⁷,
 P. Marino^{24,t}, J. Marks¹², G. Martellotti²⁶, M. Martin⁶, M. Martinelli⁴⁰, D. Martinez Santos³⁸,
 F. Martinez Vidal⁶⁸, D. Martins Tostes², L.M. Massacrier⁷, A. Massafferri¹, R. Matev³⁹,
 A. Mathad⁴⁹, Z. Mathe³⁹, C. Matteuzzi²¹, A. Mauri⁴¹, B. Maurin⁴⁰, A. Mazurov⁴⁶,
 M. McCann⁵⁴, J. McCarthy⁴⁶, A. McNab⁵⁵, R. McNulty¹³, B. Meadows⁵⁸, F. Meier¹⁰,
 M. Meissner¹², D. Melnychuk²⁹, M. Merk⁴², E. Michielin²³, D.A. Milanese⁶⁴, M.-N. Minard⁴,
 D.S. Mitzel¹², J. Molina Rodriguez⁶¹, I.A. Monroy⁶⁴, S. Monteil⁵, M. Morandin²³,
 P. Morawski²⁸, A. Mordà⁶, M.J. Morello^{24,t}, J. Moron²⁸, A.B. Morris⁵¹, R. Mountain⁶⁰,
 F. Muheim⁵¹, M. Mulder⁴², M. Mussini¹⁵, D. Müller⁵⁵, J. Müller¹⁰, K. Müller⁴¹, V. Müller¹⁰,
 P. Naik⁴⁷, T. Nakada⁴⁰, R. Nandakumar⁵⁰, A. Nandi⁵⁶, I. Nasteva², M. Needham⁵¹, N. Neri²²,
 S. Neubert¹², N. Neufeld³⁹, M. Neuner¹², A.D. Nguyen⁴⁰, C. Nguyen-Mau^{40,n}, V. Niess⁵,
 S. Nieswand⁹, R. Niet¹⁰, N. Nikitin³³, T. Nikodem¹², A. Novoselov³⁶, D.P. O'Hanlon⁴⁹,
 A. Oblakowska-Mucha²⁸, V. Obraztsov³⁶, S. Ogilvy¹⁹, O. Okhrimenko⁴⁵, R. Oldeman⁴⁸,
 C.J.G. Onderwater⁶⁹, J.M. Otalora Goicochea², A. Otto³⁹, P. Owen⁵⁴, A. Oyanguren⁶⁸,
 P.R. Pais⁴⁰, A. Palano^{14,d}, F. Palombo^{22,q}, M. Palutan¹⁹, J. Panman³⁹, A. Papanestis⁵⁰,
 M. Pappagallo⁵², L.L. Pappalardo^{17,g}, C. Pappenheimer⁵⁸, W. Parker⁵⁹, C. Parkes⁵⁵,
 G. Passaleva¹⁸, G.D. Patel⁵³, M. Patel⁵⁴, C. Patrignani^{15,e}, A. Pearce^{55,50}, A. Pellegrino⁴²,
 G. Penso^{26,k}, M. Pepe Altarelli³⁹, S. Perazzini³⁹, P. Perret⁵, L. Pescatore⁴⁶, K. Petridis⁴⁷,
 A. Petrolini^{20,h}, A. Petrov⁶⁶, M. Petruzzo^{22,q}, E. Picatoste Olloqui³⁷, B. Pietrzyk⁴, M. Pikies²⁷,
 D. Pinci²⁶, A. Pistone²⁰, A. Piucci¹², S. Playfer⁵¹, M. Plo Casasus³⁸, T. Poikela³⁹, F. Polci⁸,
 A. Poluektov^{49,35}, I. Polyakov³², E. Polycarpo², G.J. Pomery⁴⁷, A. Popov³⁶, D. Popov^{11,39},
 B. Popovici³⁰, C. Potterat², E. Price⁴⁷, J.D. Price⁵³, J. Prisciandaro³⁸, A. Pritchard⁵³,
 C. Prouve⁴⁷, V. Pugatch⁴⁵, A. Puig Navarro⁴⁰, G. Punzi^{24,p}, W. Qian⁵⁶, R. Quagliani^{7,47},
 B. Rachwal²⁷, J.H. Rademacker⁴⁷, M. Rama²⁴, M. Ramos Pernas³⁸, M.S. Rangel², I. Raniuk⁴⁴,
 G. Raven⁴³, F. Redi⁵⁴, S. Reichert¹⁰, A.C. dos Reis¹, C. Remon Alepuz⁶⁸, V. Renaudin⁷,
 S. Ricciardi⁵⁰, S. Richards⁴⁷, M. Rihl³⁹, K. Rinnert^{53,39}, V. Rives Molina³⁷, P. Robbe⁷,

A.B. Rodrigues¹, E. Rodrigues⁵⁸, J.A. Rodriguez Lopez⁶⁴, P. Rodriguez Perez⁵⁵,
A. Rogozhnikov⁶⁷, S. Roiser³⁹, V. Romanovskiy³⁶, A. Romero Vidal³⁸, J.W. Ronayne¹³,
M. Rotondo²³, T. Ruf³⁹, P. Ruiz Valls⁶⁸, J.J. Saborido Silva³⁸, E. Sadykhov³², N. Sagidova³¹,
B. Saitta^{16,f}, V. Salustino Guimaraes², C. Sanchez Mayordomo⁶⁸, B. Sanmartin Sedes³⁸,
R. Santacesaria²⁶, C. Santamarina Rios³⁸, M. Santimaria¹⁹, E. Santovetti^{25,j}, A. Sarti^{19,k},
C. Satriano^{26,s}, A. Satta²⁵, D.M. Saunders⁴⁷, D. Savrina^{32,33}, S. Schael⁹, M. Schiller³⁹,
H. Schindler³⁹, M. Schlupp¹⁰, M. Schmelling¹¹, T. Schmelzer¹⁰, B. Schmidt³⁹, O. Schneider⁴⁰,
A. Schopper³⁹, M. Schubiger⁴⁰, M.-H. Schune⁷, R. Schwemmer³⁹, B. Sciascia¹⁹, A. Sciubba^{26,k},
A. Semennikov³², A. Sergi⁴⁶, N. Serra⁴¹, J. Serrano⁶, L. Sestini²³, P. Seyfert²¹, M. Shapkin³⁶,
I. Shapoval^{17,44,g}, Y. Shcheglov³¹, T. Shears⁵³, L. Shekhtman³⁵, V. Shevchenko⁶⁶, A. Shires¹⁰,
B.G. Siddi¹⁷, R. Silva Coutinho⁴¹, L. Silva de Oliveira², G. Simi^{23,o}, M. Sirendi⁴⁸,
N. Skidmore⁴⁷, T. Skwarnicki⁶⁰, E. Smith⁵⁴, I.T. Smith⁵¹, J. Smith⁴⁸, M. Smith⁵⁵, H. Snoek⁴²,
M.D. Sokoloff⁵⁸, F.J.P. Soler⁵², D. Souza⁴⁷, B. Souza De Paula², B. Spaan¹⁰, P. Spradlin⁵²,
S. Sridharan³⁹, F. Stagni³⁹, M. Stahl¹², S. Stahl³⁹, P. Stefkova⁴⁰, S. Stefkova⁵⁴, O. Steinkamp⁴¹,
O. Stenyakin³⁶, S. Stevenson⁵⁶, S. Stoica³⁰, S. Stone⁶⁰, B. Storaci⁴¹, S. Stracka^{24,t},
M. Straticiu³⁰, U. Straumann⁴¹, L. Sun⁵⁸, W. Sutcliffe⁵⁴, K. Swientek²⁸, V. Syropoulos⁴³,
M. Szczekowski²⁹, T. Szumlak²⁸, S. T'Jampens⁴, A. Tayduganov⁶, T. Tekampe¹⁰,
G. Tellarini^{17,g}, F. Teubert³⁹, C. Thomas⁵⁶, E. Thomas³⁹, J. van Tilburg⁴², V. Tisserand⁴,
M. Tobin⁴⁰, S. Tolk⁴⁸, L. Tomassetti^{17,g}, D. Tonelli³⁹, S. Topp-Joergensen⁵⁶, F. Toriello⁶⁰,
E. Tournefier⁴, S. Tourneur⁴⁰, K. Trabelsi⁴⁰, M. Traill⁵², M.T. Tran⁴⁰, M. Tresch⁴¹,
A. Trisovic³⁹, A. Tsaregorodtsev⁶, P. Tsopelas⁴², A. Tully⁴⁸, N. Tuning⁴², A. Ukleja²⁹,
A. Ustyuzhanin^{67,66}, U. Uwer¹², C. Vacca^{16,39,f}, V. Vagnoni^{15,39}, S. Valat³⁹, G. Valenti¹⁵,
A. Vallier⁷, R. Vazquez Gomez¹⁹, P. Vazquez Regueiro³⁸, S. Vecchi¹⁷, M. van Veghel⁴²,
J.J. Velthuis⁴⁷, M. Veltri^{18,r}, G. Veneziano⁴⁰, A. Venkateswaran⁶⁰, M. Vesterinen¹², B. Viaud⁷,
D. Vieira¹, M. Vieites Diaz³⁸, X. Vilasis-Cardona^{37,m}, V. Volkov³³, A. Vollhardt⁴¹, B. Voneki³⁹,
D. Voong⁴⁷, A. Vorobyev³¹, V. Vorobyev³⁵, C. Voß⁶⁵, J.A. de Vries⁴², C. Vázquez Sierra³⁸,
R. Waldi⁶⁵, C. Wallace⁴⁹, R. Wallace¹³, J. Walsh²⁴, J. Wang⁶⁰, D.R. Ward⁴⁸, H.M. Wark⁵³,
N.K. Watson⁴⁶, D. Websdale⁵⁴, A. Weiden⁴¹, M. Whitehead³⁹, J. Wicht⁴⁹, G. Wilkinson^{56,39},
M. Wilkinson⁶⁰, M. Williams³⁹, M.P. Williams⁴⁶, M. Williams⁵⁷, T. Williams⁴⁶, F.F. Wilson⁵⁰,
J. Wimberley⁵⁹, J. Wishahi¹⁰, W. Wislicki²⁹, M. Witek²⁷, G. Wormser⁷, S.A. Wotton⁴⁸,
K. Wraight⁵², S. Wright⁴⁸, K. Wyllie³⁹, Y. Xie⁶³, Z. Xu⁴⁰, Z. Yang³, H. Yin⁶³, J. Yu⁶³,
X. Yuan³⁵, O. Yushchenko³⁶, M. Zangoli¹⁵, K.A. Zarebski⁴⁶, M. Zavertyaev^{11,c}, L. Zhang³,
Y. Zhang⁷, Y. Zhang⁶², A. Zhelezov¹², Y. Zheng⁶², A. Zhokhov³², V. Zhukov⁹, S. Zucchelli¹⁵.

¹ Centro Brasileiro de Pesquisas Físicas (CBPF), Rio de Janeiro, Brazil

² Universidade Federal do Rio de Janeiro (UFRJ), Rio de Janeiro, Brazil

³ Center for High Energy Physics, Tsinghua University, Beijing, China

⁴ LAPP, Université Savoie Mont-Blanc, CNRS/IN2P3, Annecy-Le-Vieux, France

⁵ Clermont Université, Université Blaise Pascal, CNRS/IN2P3, LPC, Clermont-Ferrand, France

⁶ CPPM, Aix-Marseille Université, CNRS/IN2P3, Marseille, France

⁷ LAL, Université Paris-Sud, CNRS/IN2P3, Orsay, France

⁸ LPNHE, Université Pierre et Marie Curie, Université Paris Diderot, CNRS/IN2P3, Paris, France

⁹ I. Physikalisches Institut, RWTH Aachen University, Aachen, Germany

¹⁰ Fakultät Physik, Technische Universität Dortmund, Dortmund, Germany

¹¹ Max-Planck-Institut für Kernphysik (MPIK), Heidelberg, Germany

¹² Physikalisches Institut, Ruprecht-Karls-Universität Heidelberg, Heidelberg, Germany

¹³ School of Physics, University College Dublin, Dublin, Ireland

¹⁴ Sezione INFN di Bari, Bari, Italy

- ¹⁵ *Sezione INFN di Bologna, Bologna, Italy*
- ¹⁶ *Sezione INFN di Cagliari, Cagliari, Italy*
- ¹⁷ *Sezione INFN di Ferrara, Ferrara, Italy*
- ¹⁸ *Sezione INFN di Firenze, Firenze, Italy*
- ¹⁹ *Laboratori Nazionali dell'INFN di Frascati, Frascati, Italy*
- ²⁰ *Sezione INFN di Genova, Genova, Italy*
- ²¹ *Sezione INFN di Milano Bicocca, Milano, Italy*
- ²² *Sezione INFN di Milano, Milano, Italy*
- ²³ *Sezione INFN di Padova, Padova, Italy*
- ²⁴ *Sezione INFN di Pisa, Pisa, Italy*
- ²⁵ *Sezione INFN di Roma Tor Vergata, Roma, Italy*
- ²⁶ *Sezione INFN di Roma La Sapienza, Roma, Italy*
- ²⁷ *Henryk Niewodniczanski Institute of Nuclear Physics Polish Academy of Sciences, Kraków, Poland*
- ²⁸ *AGH - University of Science and Technology, Faculty of Physics and Applied Computer Science, Kraków, Poland*
- ²⁹ *National Center for Nuclear Research (NCBJ), Warsaw, Poland*
- ³⁰ *Horia Hulubei National Institute of Physics and Nuclear Engineering, Bucharest-Magurele, Romania*
- ³¹ *Petersburg Nuclear Physics Institute (PNPI), Gatchina, Russia*
- ³² *Institute of Theoretical and Experimental Physics (ITEP), Moscow, Russia*
- ³³ *Institute of Nuclear Physics, Moscow State University (SINP MSU), Moscow, Russia*
- ³⁴ *Institute for Nuclear Research of the Russian Academy of Sciences (INR RAN), Moscow, Russia*
- ³⁵ *Budker Institute of Nuclear Physics (SB RAS) and Novosibirsk State University, Novosibirsk, Russia*
- ³⁶ *Institute for High Energy Physics (IHEP), Protvino, Russia*
- ³⁷ *Universitat de Barcelona, Barcelona, Spain*
- ³⁸ *Universidad de Santiago de Compostela, Santiago de Compostela, Spain*
- ³⁹ *European Organization for Nuclear Research (CERN), Geneva, Switzerland*
- ⁴⁰ *Ecole Polytechnique Fédérale de Lausanne (EPFL), Lausanne, Switzerland*
- ⁴¹ *Physik-Institut, Universität Zürich, Zürich, Switzerland*
- ⁴² *Nikhef National Institute for Subatomic Physics, Amsterdam, The Netherlands*
- ⁴³ *Nikhef National Institute for Subatomic Physics and VU University Amsterdam, Amsterdam, The Netherlands*
- ⁴⁴ *NSC Kharkiv Institute of Physics and Technology (NSC KIPT), Kharkiv, Ukraine*
- ⁴⁵ *Institute for Nuclear Research of the National Academy of Sciences (KINR), Kyiv, Ukraine*
- ⁴⁶ *University of Birmingham, Birmingham, United Kingdom*
- ⁴⁷ *H.H. Wills Physics Laboratory, University of Bristol, Bristol, United Kingdom*
- ⁴⁸ *Cavendish Laboratory, University of Cambridge, Cambridge, United Kingdom*
- ⁴⁹ *Department of Physics, University of Warwick, Coventry, United Kingdom*
- ⁵⁰ *STFC Rutherford Appleton Laboratory, Didcot, United Kingdom*
- ⁵¹ *School of Physics and Astronomy, University of Edinburgh, Edinburgh, United Kingdom*
- ⁵² *School of Physics and Astronomy, University of Glasgow, Glasgow, United Kingdom*
- ⁵³ *Oliver Lodge Laboratory, University of Liverpool, Liverpool, United Kingdom*
- ⁵⁴ *Imperial College London, London, United Kingdom*
- ⁵⁵ *School of Physics and Astronomy, University of Manchester, Manchester, United Kingdom*
- ⁵⁶ *Department of Physics, University of Oxford, Oxford, United Kingdom*
- ⁵⁷ *Massachusetts Institute of Technology, Cambridge, MA, United States*
- ⁵⁸ *University of Cincinnati, Cincinnati, OH, United States*
- ⁵⁹ *University of Maryland, College Park, MD, United States*
- ⁶⁰ *Syracuse University, Syracuse, NY, United States*
- ⁶¹ *Pontifícia Universidade Católica do Rio de Janeiro (PUC-Rio), Rio de Janeiro, Brazil, associated to ²*
- ⁶² *University of Chinese Academy of Sciences, Beijing, China, associated to ³*
- ⁶³ *Institute of Particle Physics, Central China Normal University, Wuhan, Hubei, China, associated to ³*
- ⁶⁴ *Departamento de Física, Universidad Nacional de Colombia, Bogota, Colombia, associated to ⁸*

- ⁶⁵ *Institut für Physik, Universität Rostock, Rostock, Germany, associated to* ¹²
⁶⁶ *National Research Centre Kurchatov Institute, Moscow, Russia, associated to* ³²
⁶⁷ *Yandex School of Data Analysis, Moscow, Russia, associated to* ³²
⁶⁸ *Instituto de Física Corpuscular (IFIC), Universitat de Valencia-CSIC, Valencia, Spain, associated to* ³⁷
⁶⁹ *Van Swinderen Institute, University of Groningen, Groningen, The Netherlands, associated to* ⁴²

- ^a *Universidade Federal do Triângulo Mineiro (UFMT), Uberaba-MG, Brazil*
^b *Laboratoire Leprince-Ringuet, Palaiseau, France*
^c *P.N. Lebedev Physical Institute, Russian Academy of Science (LPI RAS), Moscow, Russia*
^d *Università di Bari, Bari, Italy*
^e *Università di Bologna, Bologna, Italy*
^f *Università di Cagliari, Cagliari, Italy*
^g *Università di Ferrara, Ferrara, Italy*
^h *Università di Genova, Genova, Italy*
ⁱ *Università di Milano Bicocca, Milano, Italy*
^j *Università di Roma Tor Vergata, Roma, Italy*
^k *Università di Roma La Sapienza, Roma, Italy*
^l *AGH - University of Science and Technology, Faculty of Computer Science, Electronics and Telecommunications, Kraków, Poland*
^m *LIFAELS, La Salle, Universitat Ramon Llull, Barcelona, Spain*
ⁿ *Hanoi University of Science, Hanoi, Viet Nam*
^o *Università di Padova, Padova, Italy*
^p *Università di Pisa, Pisa, Italy*
^q *Università degli Studi di Milano, Milano, Italy*
^r *Università di Urbino, Urbino, Italy*
^s *Università della Basilicata, Potenza, Italy*
^t *Scuola Normale Superiore, Pisa, Italy*
^u *Università di Modena e Reggio Emilia, Modena, Italy*